

Physical Biology



PAPER

OPEN ACCESS

RECEIVED
3 February 2023

REVISED
2 May 2023

ACCEPTED FOR PUBLICATION
24 May 2023

PUBLISHED
12 June 2023

Original content from this work may be used under the terms of the [Creative Commons Attribution 4.0 licence](https://creativecommons.org/licenses/by/4.0/).

Any further distribution of this work must maintain attribution to the author(s) and the title of the work, journal citation and DOI.



Fractal dimension to characterize interactions between blood and lymphatic endothelial cells

Donghyun Paul Jeong^{1,2} , Daniel Montes^{1,3}, Hsueh-Chia Chang^{1,2,3,4,5} and Donny Hanjaya-Putra^{1,2,3,4,5,*}

¹ Bioengineering Graduate Program, University of Notre Dame, Notre Dame, IN 46556, United States of America

² Aerospace and Mechanical Engineering, University of Notre Dame, Notre Dame, IN 46556, United States of America

³ Chemical and Biomolecular Engineering, University of Notre Dame, Notre Dame, IN 46556, United States of America

⁴ Harper Cancer Research Institute, University of Notre Dame, Notre Dame, IN 46556, United States of America

⁵ Center for Stem Cell and Regenerative Medicine, University of Notre Dame, Notre Dame, IN 46556, United States of America

* Author to whom any correspondence should be addressed.

E-mail: dputra1@nd.edu

Keywords: fractal dimension, morphogenesis, cell migration, blood and lymphatic endothelial cells

Supplementary material for this article is available [online](#)

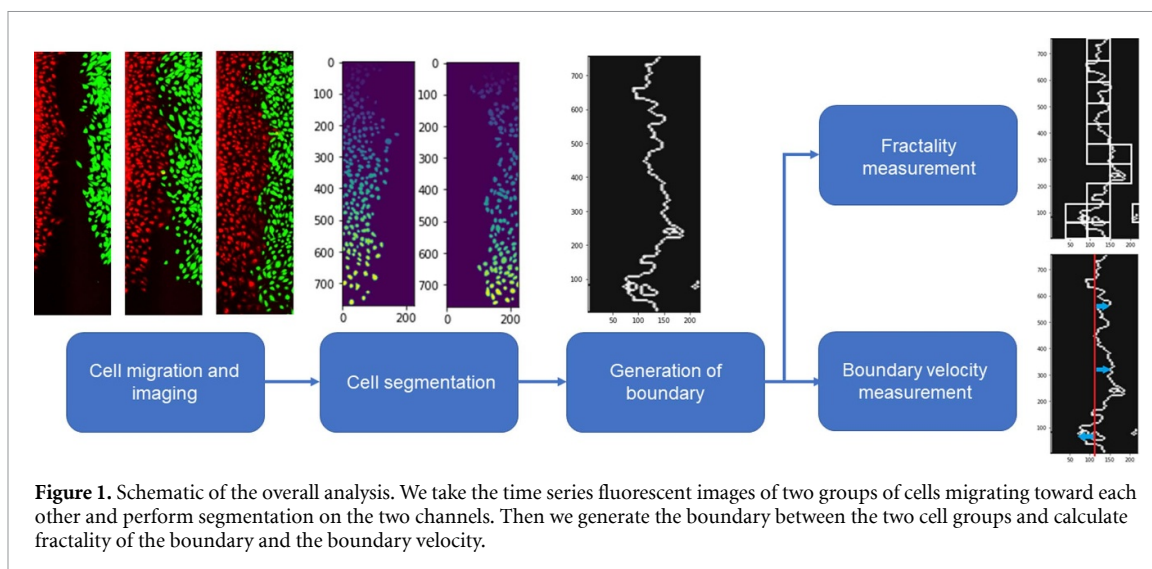
Abstract

Spatial patterning of different cell types is crucial for tissue engineering and is characterized by the formation of sharp boundary between segregated groups of cells of different lineages. The cell–cell boundary layers, depending on the relative adhesion forces, can result in kinks in the border, similar to fingering patterns between two viscous partially miscible fluids which can be characterized by its fractal dimension. This suggests that mathematical models used to analyze the fingering patterns can be applied to cell migration data as a metric for intercellular adhesion forces. In this study, we develop a novel computational analysis method to characterize the interactions between blood endothelial cells (BECs) and lymphatic endothelial cells (LECs), which form segregated vasculature by recognizing each other through podoplanin. We observed indiscriminate mixing with LEC–LEC and BEC–BEC pairs and a sharp boundary between LEC–BEC pair, and fingering-like patterns with pseudo-LEC–BEC pairs. We found that the box counting method yields fractal dimension between 1 for sharp boundaries and 1.3 for indiscriminate mixing, and intermediate values for fingering-like boundaries. We further verify that these results are due to differential affinity by performing random walk simulations with differential attraction to nearby cells and generate similar migration pattern, confirming that higher differential attraction between different cell types result in lower fractal dimensions. We estimate the characteristic velocity and interfacial tension for our simulated and experimental data to show that the fractal dimension negatively correlates with capillary number (Ca), further indicating that the mathematical models used to study viscous fingering pattern can be used to characterize cell–cell mixing. Taken together, these results indicate that the fractal analysis of segregation boundaries can be used as a simple metric to estimate relative cell–cell adhesion forces between different cell types.

1. Introduction

During embryonic development, cells bound for different fates grow in close proximity to each other, and yet develop well-defined boundaries between separate tissues [1–3]. While undergoing rapid growth and differentiation, cells also retain their pattern

forming abilities that drive morphogenesis and tissue formation [4–6]. Loss of cadherin function in embryogenesis, which is responsible for cell segregation, leads to a failure to form distinct compartments in the embryo and therefore causes embryonic lethality, highlighting the importance of cell–cell boundary formation in tissue morphogenesis [7, 8].



In order to achieve clear boundary formation, cells use a combination of differential adhesion, selective avoidance, and cortical tension to form boundaries [9, 10]. Differential adhesion is achieved through surface receptors which selectively recognize cells and form tighter bonds with them through the cadherin family of molecules [11–13]. Cells also develop selective repulsion through Eph-ephrin-guided mechanism, which has also been reported to play a role in cell segregation [14, 15]. Actomyosin also plays a role in cell segregation through mediation of cortical tension which affects cell cytosol to reshape boundaries [16, 17]. These factors contribute to the cells selectively forming tighter or looser bonds with surrounding cells, leading to a differential in affinity between cells of the same type and different type [9]. The degree of differential in affinity determines the crispness of the borders between two cells types, with higher differential affinity leading to straighter borders [18]. Similar to two immiscible fluid–fluid surface, high degree of selective preference for cells of its own type leads to energetical unfavourability of rough, fuzzy surfaces and formation of straight borders to minimize the contact with cells of the same type [19].

This formation of straight, clear borders is important in stem cell-based tissue engineering, since stem cell-derived mature cells often suffer from immaturity and lower marker expression compared to their native mature counterparts [20–22]. Therefore, in tissue engineering applications requiring more than one type of cell, for example in vascularized tissue engineering involving the endothelial and target tissue-specific cells, the recognition ability of cells and the resulting differential affinity is crucial for free energy-driven self-organization of cells [23–26]. In order to predict the ability of two or more types of human induced pluripotent stem cell-derived cells to self-assemble into tissues, measuring the differential affinity between different cell types

is crucial [2, 22]. Numerous studies have proposed mathematical models to explain the collective migration and organization behavior of cells [27]. A study by Mark *et al* proposed a dynamic instability model to predict cell–cell boundary formation which is solely affected by cell shape and motility without accounting for chemical gradients [28]. Another study by Kopf and Pismen proposed modeling of the cell–cell boundary as an elastic continuum that can respond to chemical and mechanical stimuli [29]. Here, we put forth our mathematical model to characterize cell–cell boundary inspired by the field of petroleum engineering.

In this study, we propose the use of fractal dimension of the cell–cell boundary after two cell types are allowed to migrate towards each other (figure 1). Fractal dimension analysis has been widely used to study the geometric arrangements of various substances and materials, including tissues during development [30–33]. Some fractals are self-similar, meaning they exhibit geometric similarity at any scale, and there are several techniques and mathematical approaches that can be used to generate and describe these self-similar geometries [34]. However, many natural architectures do not show self-similarity, but instead exhibit a scale-limited similar pattern, making them pseudo-fractals [35]. These can also be analyzed using the same mathematical tools as self-similar fractals [35, 36].

Pseudo-fractals are commonly observed during the displacement of immiscible fluids in porous media, such as in enhanced oil recovery (EOR) processes [37, 38]. During EOR, capillary forces produce an interphase between the immiscible phases due to interfacial tension, velocity, and viscosity [39]. These forces can shape the boundary, resulting in straight and clear interphases or viscous fingering like patterns with pseudo-fractal behavior [40]. Similarly, the interaction of two different cell lines during tissue development is governed by differential

affinity and altering this affinity can create different boundary patterns that can be analyzed using fractal dimension analysis. For example, in our previous study we demonstrated that surface receptor podoplanin is responsible for the distinct capillaries formed by blood endothelial cells (BECs) and lymphatic endothelial cells (LECs) [41]. To further explain the interaction between BECs and LECs, here we showed that fractal dimension analysis can be used to characterize BECs and LECs interactions during cell migration, an essential step toward blood and lymphatic tube formation [23, 42].

2. Methods

2.1. Cell segmentation and boundary definition

We utilized the data published by Jeong *et al* which included timeseries fluorescent images of BECs and LECs stained with different membrane staining dye and allowed to migrate towards each other [41]. We performed manual background subtraction by setting lower threshold to remove the background fluorescence. Videos over 25 MB in size were cropped into two separate videos to avoid problems associated with handling large file sizes. The timeseries images were segmented using Cellpose, a publicly available Python package that uses machine learning algorithm to segment the cells [43]. We used the Cyto model with an estimated diameter of 10 pixels to generate masks corresponding to the location of each cell for both types of cells. We then calculated the center of each mask of the cell to generate a single location point for each cell. The locations of cells for each timepoint were used as input data to generate the boundary. We generated a NumPy meshgrid of the same size as the input video and used SciPy's K-Neighbor Classifier for each point to classify each point into either region 1 or 2 based on the number of cells nearest to it. Then we defined the boundary layer as the set of pixels in region 1 which bordered region 2 (figure 2(A)).

2.2. Box counting method

We determined the fractality of the boundary layer through box counting method. The image of the boundary layer, where the boundary pixels are assigned the value of 1 and non-boundary pixels 0, was used as the input to the algorithm. We generated a list of square box sizes from 2 pixels in length to half of the width of the video. Then we calculate the number of boxes that contain at least one border pixel for each box size, then plot the number of positive counts against the box sizes. We used NumPy's polyfit function to generate the slope of the log–log values of box sizes and positive counts, which corresponds to the Hausdorff dimension of the boundary.

2.3. Boundary displacement calculations

We calculated the boundary layer velocity by estimating the average displacement of the boundary pixels

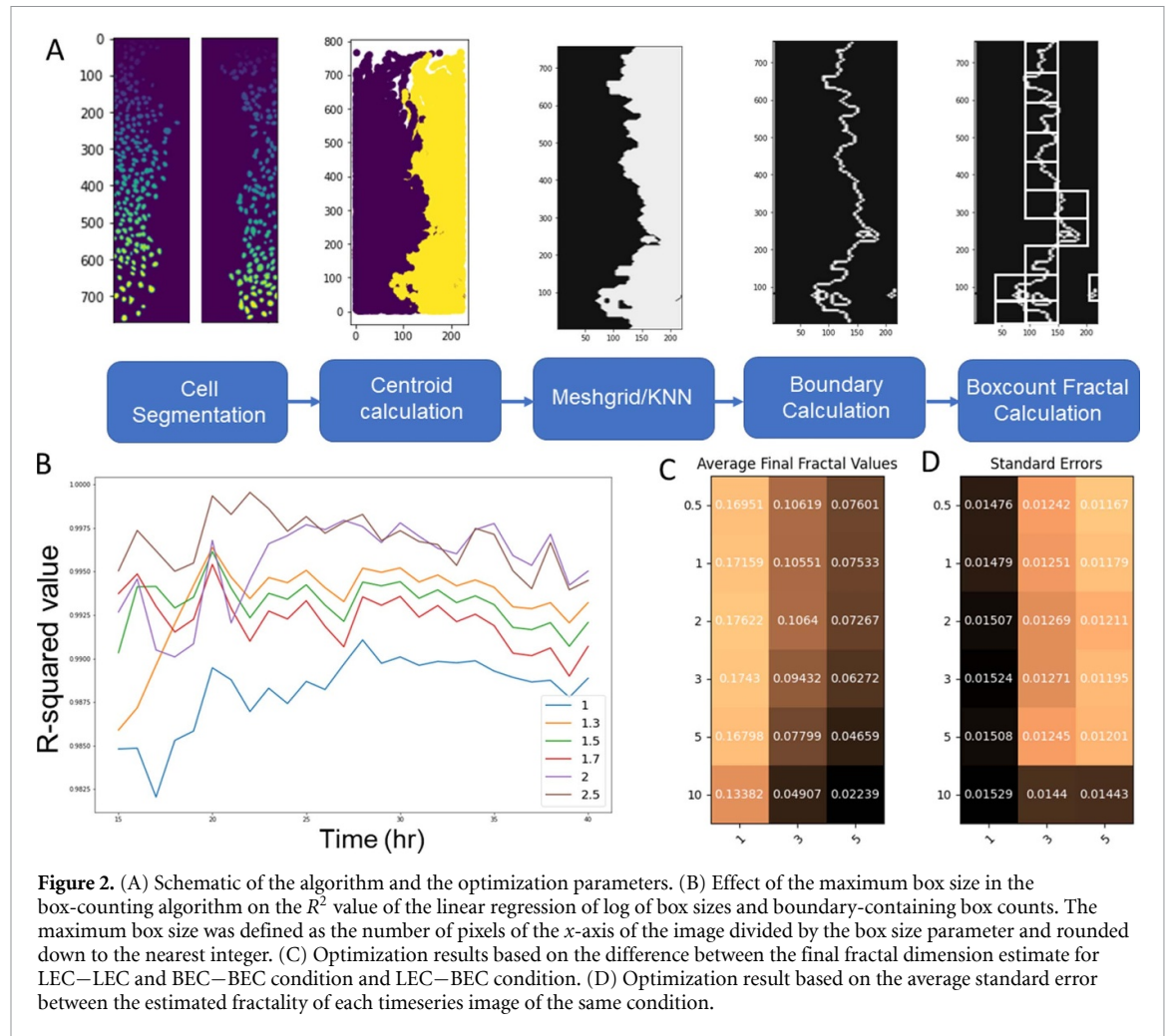
from the initial position. The initial position was defined as the boundary layer when the cells first made contact, as visibly confirmed through fluorescent images. For each y -coordinate along the boundary, the absolute value of the deviation of the boundary layer from the initial position at that y -coordinate was averaged throughout the entire boundary. If there are multiple boundary layer pixels within a given y -coordinate, then the greatest value was taken. The average displacement was taken as the displacement of the boundary layer. To calculate the velocity, the boundary layer displacements were averaged over 10 most recent timepoints to smooth out the noise in the displacement.

2.4. Optimization of the algorithm

We optimized three parameters in our overall algorithm: the maximum box size in the box-counting algorithm, the coarseness of the NumPy meshgrid, and the number of neighbors during the K-nearest neighbors classification step. In generating the list of different sizes of boxes to use, we found that setting the largest box size to equal the width of the video resulted in box counts that deviated from the linear expectation. Therefore, we calculated the R -squared value of the linear fit resulting from box counting methods where the largest box size was set to the number of pixels of the x -axis of the image divided by box-size parameter b rounded to the nearest integer (figure 2(B)). We found that the optimum value of b was 2, meaning that the largest box size in our algorithm was half of the width of the video. We also determined the coarseness of the meshgrid by changing the number of points in the meshgrid each pixel would be represented by. We tested compression factors of 0.5, 1, 2, 3, 5, and 10, which correspond to the number of pixels each point in meshgrid represents. We also optimized for the different number of neighbors in the K-nearest neighbor algorithm. We used two metrics for optimizing these parameters: the difference in the average final fractal value between the LEC–LEC and BEC–LEC conditions and the average standard error for those two conditions. We want to maximize the difference in final fractal value and minimize the standard error to achieve the best algorithm that can discriminate between LEC–LEC and LEC–BEC condition while also yielding consistent results. Based on the results, we see that the meshgrid compression of 2 achieves optimal balance between the two metrics, and we observe a greater degree of discrimination and variability with lower number of neighbors (figures 2(C) and (D)). Therefore, for all further work, we used 1 nearest neighbor and meshgrid factor of 2.

2.5. Random walk simulation

We generated a NumPy array of 400 cells each of type 1 and 2, each consisting of x - and y -coordinate bound within 30 by 50 grid. The cells were initially



organized in a block pattern, occupying 8 columns of 50 cells along the two edges of the grid. We designed a modified Gillespie algorithm by defining the relative probability of a cell moving into each of the four adjacent spaces. The simulation incorporated five parameters: p_{m1} , p_{m2} , a_{l1} , a_{l2} , and a_d . Parameters p_{m1} and p_{m2} defined the probability of a cell moving within a given timeframe, and for all simulations they were set to 0.95 for both cell types. Parameters a_{l1} and a_{l2} defined the effect of a cell of the same type on the probability of the cell moving to the adjacent space respectively for cell type 1 and 2. Parameter a_d defined the effect of the opposite cell type on the probability of cell movement. The cumulative effect of the like and dislike cells was calculated by multiplying the individual effects together. Therefore, a value greater than 1 indicates affinity between two cells, while a value of less than 1 indicates repulsion. We did not incorporate the impact of an immediately adjacent cell on the probability of the cell moving within a timepoint. A cell was forbidden from moving into a space that was already occupied by another cell or off the grid. For our simulation, we assumed no cell division or death. The overall probability of a cell of type 1 moving in direction i is therefore represented as

$$p_{i, \text{cell}1} = p_{m1} \left(\frac{q_k}{\sum_{j=0}^3 q_j} \right)$$

$$q_j = a_{l1}^{n_l} a_d^{n_d} r$$

where n_l and n_d respectively represents the number of same and opposite type of cells adjacent to the space the cell might move to, and r is a binary value which is equal to 0 if the spot is occupied or exists at the edge, and 1 if available. Calculations for q was performed for each of the four spaces a cell can move into.

For each timepoint, the probability for each cell was calculated, and a random number generator determined the movement of each cell. For cells which could not move to any space in a given timepoint, the q values were all set to 0. The calculations were performed sequentially, where the previous cell was allowed to finish its movement before the probability was calculated for the next cell in order to prevent the probability of two cells moving into the same space. The order of the cells were randomly shuffled at each timepoint. The updated cell locations were saved as a NumPy array of x - and y -coordinates and used for subsequent fractal analysis using the same boundary defining and box counting methods described above.

3. Results

3.1. Lower differential affinity results in higher final fractality value

We used the data we previously published in the journal *Cellular Molecular and Bioengineering*, where we reported that podoplanin is responsible for the selective cell–cell interaction between BECs and LECs [41]. The LECs and BECs preferentially form tight junctions with only the cells of their own kind during capillary formation, allowing the separation of the blood and the lymph. We found that this recognition is dependent on the expression of podoplanin in LECs, which is consistent with previous observations [44–46]. Therefore, we found that podoplanin-knockout LECs (referred to as Δ LEC) act somewhat similarly to BECs and are recognized as pseudo-BECs.

As previously described, we performed migration assays with BECs and LECs stained in two different live cell tracking fluorescent dyes [41]. We seeded BECs on one side and either LECs, BECs, or Δ LECs on the other side and allowed the gap to close by cells migrating toward each other. We segmented the cell data and defined the boundary between the two groups of cells and calculated the fractality over time (figure 1). We found that the fractality of the boundary between two like cells, which exhibit no preference towards cells of its own side, increases to around 1.25, while the fractality of the two opposite cells remains around 1.05 (figures 3(A) and (B)). We only calculated the fractality after 8 h of migration when the gap fully closed, and the cells came into contact with each other. We also performed a similar analysis on the knockout condition and found the final fractal value to be around 1.15 (figure 3(C)). The fractal values correspond with the known affinity of BECs to other BECs versus LECs. We also expect the pseudo-LECs which express some BEC-like characteristics to have affinity for BECs that is between LECs and BECs, which also corresponds to the fractal values. However, it is challenging to measure the exact affinity of BECs to other BECs and LECs, which means the exact differential affinity is not measured. All *in vitro* cell migration assays were performed for 24 h at most, since beyond that point, cells will begin to undergo division and therefore the resulting fractality is not only a function of differential affinity, but also cell proliferative potential [42, 47].

3.2. Random walk simulation

In order to measure the effect of differential affinity on fractality, we designed a random walk simulation to model the movement of the two types of cells. We tested five conditions: for all conditions, the probabilities of movement for both cells were set to 0.95, and the attractive force between the two like cells were set to 1.5 for both cells. For a_d values, we tested 1.5 to simulate the BEC–BEC condition and 0.5, 0.2, 0.1, and

0.05 to simulate varying levels of differential affinity between BECs and LECs (supplemental figure 1). We ran the simulation for 80 timepoints and found that the gap is mostly closed by timepoint 30. We have empirically determined that 80 timepoints is the minimum timepoints required for all tested conditions to reach approximately zero boundary velocity when averaged over 5 consecutive timepoints. From timepoint 30–80, we performed the fractality analysis and found that greater differential affinity results in significantly lower fractality value (figures 4(A)–(C)). For a_d value of 1.5, the fractal value reached close to 1.30, similarly to our BEC–BEC condition, and for 0.05, the fractal value remained close to 1.05, analogous to BEC–LEC condition. For a_d value of 0.2, the fractal dimension reached approximately 1.15 similarly to our BEC– Δ LEC condition. We also calculated the boundary layer displacement for each of these conditions and found that higher differential adhesion led to lower boundary layer displacement as expected (figures 4(D)–(F)).

3.3. Relationship with the capillary number

To determine if our analysis of the fractal dimension is analogous to viscous fingering, we analyzed the relationship between capillary number and fractality in our simulations. It has been previously reported that in viscous fingering, Ca is negatively correlated with fractality [48]. In biological applications, unlike in petroleum engineering, the capillary number does not vary by large magnitudes, therefore, we assume local linear relationship between fractality and capillary number

$$f = -mCa + b = -m\frac{\mu V}{\sigma} + b$$

where V represents boundary velocity, σ is the interfacial tension, μ is the viscosity, and m and b represents constants. We expected to see that the fractality of the boundary would be close to 1 when the cells are moving rapidly to close the gap, which is when the cells are moving at their maximum speed in absence of obstacles. At point of initial contact, when the boundary is essentially a one-dimensional straight line, the velocity would also equal V_{\max} if we assume continuity of velocity. Effectively, we observe that boundary velocity acts as a proxy for time, transitioning from initial V_{\max} to final velocity of 0 as cells lose the driving force behind migration as the cell density reaches equilibrium. Therefore, we expected fractal value to be close to 1 at maximum velocity, which is at initial timepoint, which allowed us to make the following prediction:

$$\lim_{V \rightarrow V_{\max}} f = 1.$$

Likewise, we can assume that the viscous fingering will reach equilibrium at distant timepoint, which is when the boundary velocity will reach 0. At this point,

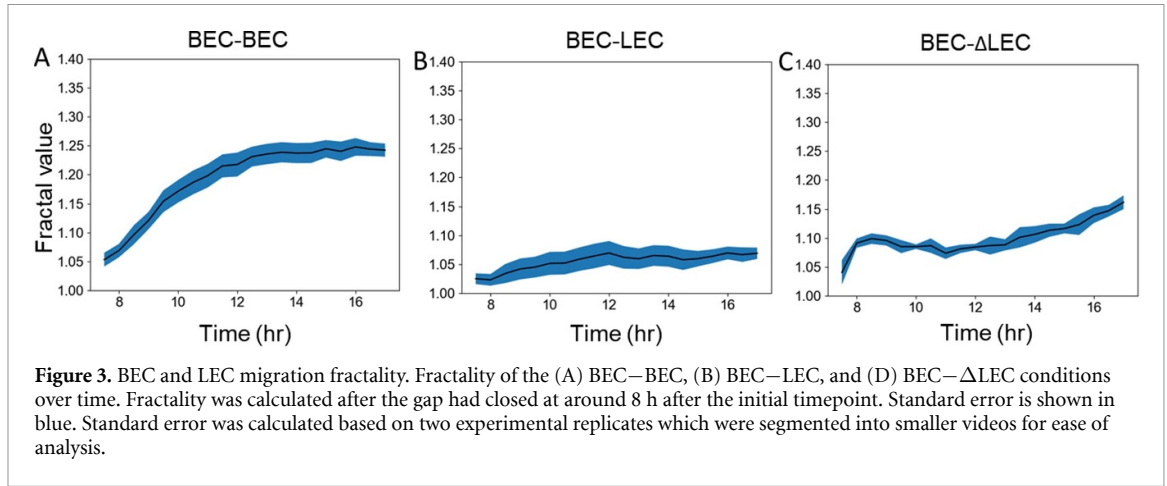


Figure 3. BEC and LEC migration fractality. Fractality of the (A) BEC–BEC, (B) BEC–LEC, and (D) BEC– Δ LEC conditions over time. Fractality was calculated after the gap had closed at around 8 h after the initial timepoint. Standard error is shown in blue. Standard error was calculated based on two experimental replicates which were segmented into smaller videos for ease of analysis.

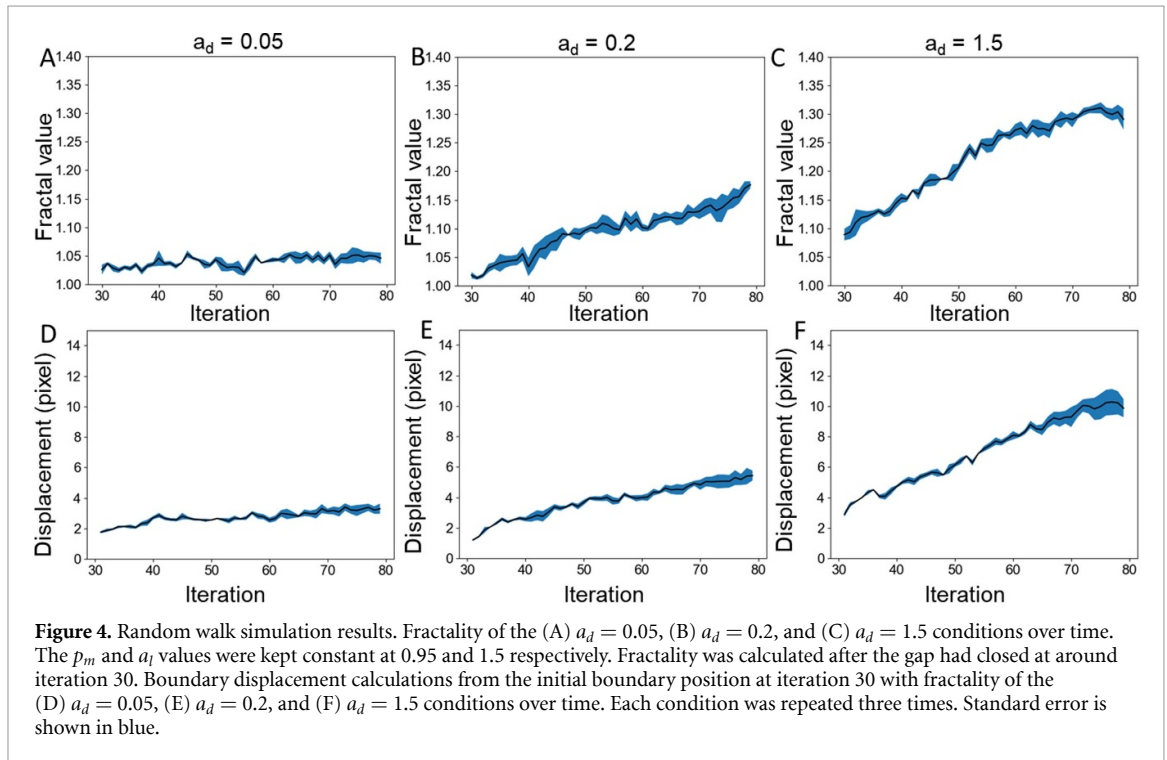


Figure 4. Random walk simulation results. Fractality of the (A) $a_d = 0.05$, (B) $a_d = 0.2$, and (C) $a_d = 1.5$ conditions over time. The p_m and a_i values were kept constant at 0.95 and 1.5 respectively. Fractality was calculated after the gap had closed at around iteration 30. Boundary displacement calculations from the initial boundary position at iteration 30 with fractality of the (D) $a_d = 0.05$, (E) $a_d = 0.2$, and (F) $a_d = 1.5$ conditions over time. Each condition was repeated three times. Standard error is shown in blue.

the fractality would no longer change, meaning this would be our final fractal value. Therefore, we generate another prediction:

$$\lim_{V \rightarrow 0} f = f_{\text{final}}.$$

Therefore, we see that if for all conditions, as V approaches V_{max} the fractality must approach 1. This means we can express fractality as

$$f = -m \frac{\mu V}{\sigma} + 1 + m \frac{\mu V_{\text{max}}}{\sigma},$$

where m is a constant. We can therefore predict that the final fractal value will have the following relationship:

$$f_{\text{final}} = m \frac{\mu V_{\text{max}}}{\sigma} + 1 \propto \frac{1}{\sigma}.$$

We also predicted that the rate of change of fractality with velocity to be approximately

$$-\frac{df}{dV} = m \frac{\mu}{\sigma} \propto \frac{1}{\sigma}.$$

Based on this, we estimated that the final fractal value would be inversely proportional to the differential affinity or surface tension, and that the rate of change of fractality with velocity would be negatively correlated with differential affinity. Using the simulated cells, we found that these relationships are indeed shown to be true. For the model parameters, we held constant the viscosity μ , analogous to the $p_{m1,2}$ parameter in our model, and estimated that interfacial tension σ would be analogous to a_1/a_d . This means that lower a_d value indicates stronger repulsion by the other cell type and therefore results in higher surface tension. In our simulations, we

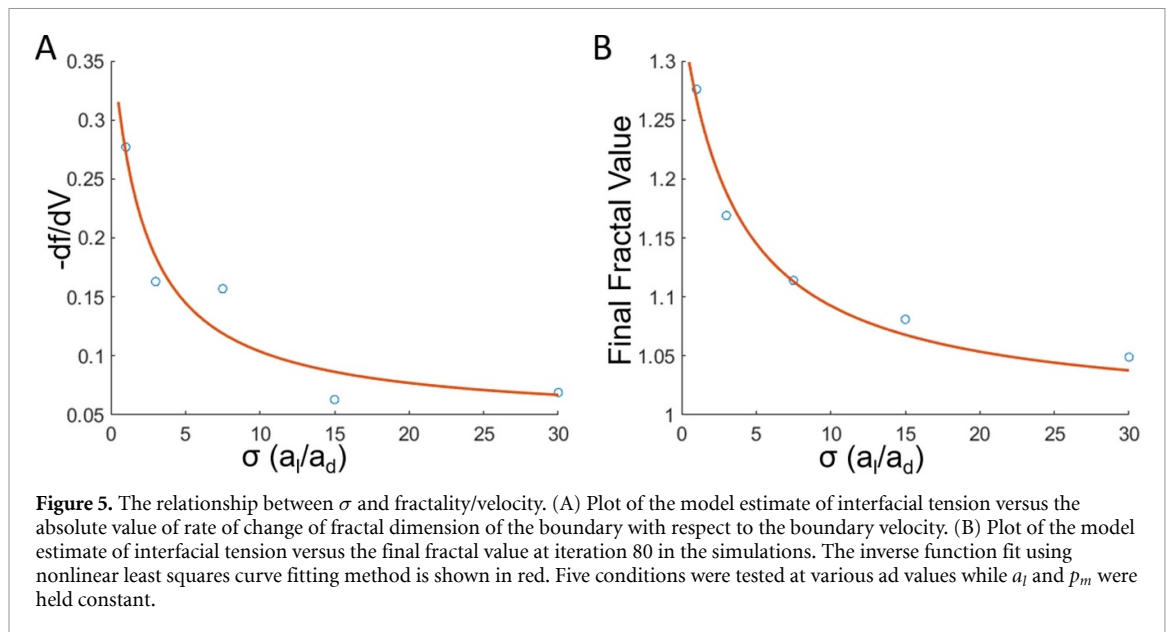


Figure 5. The relationship between σ and fractality/velocity. (A) Plot of the model estimate of interfacial tension versus the absolute value of rate of change of fractal dimension of the boundary with respect to the boundary velocity. (B) Plot of the model estimate of interfacial tension versus the final fractal value at iteration 80 in the simulations. The inverse function fit using nonlinear least squares curve fitting method is shown in red. Five conditions were tested at various a_d values while a_l and p_m were held constant.

found that both the final fractal value and the slope of fractal-velocity plot were both inversely proportional to σ . We fit the data we derived from the random walk simulations with inverse proportion equation through non-linear least squares fitting method and derived the following relations:

$$f_{\text{final}} = \frac{1.2737}{\sigma + 3.7595} + 1$$

$$-\frac{df}{dV} = \frac{0.7181}{\sigma + 2.1533} + 0.0447.$$

We achieved the square norm of the residual values of 0.0007 and 0.0025 respectively for the σ vs final fractal value and σ vs negative of slope values (figures 5(A) and (B)). To confirm that the calculated values are best fit by the inverse function, we also fit the data to linear, second-order polynomial, exponential decay and confirmed that the inverse function yields the lowest norm of the residual (supplemental figure 2). These results indicate that our fractal analysis responds similarly to fractality of viscous fingering systems. Since there is a strong inverse relationship between the final fractal value and the interfacial tension, this suggests that fractal dimension measurement of the cell–cell boundary can be used as a relative measure of cell–cell adhesion.

4. Discussion

In this study, we have used fractality of the boundary between two types of cells to estimate the differential affinity between them. We modeled the cells as a system consisting of two partially miscible fluids allowed to move toward each other in a 2D surface, which can result in viscous fingering pattern. It is important to note that as the cells from single monolayers, we do not expect the vertical dimension to affect our

conclusion. While random walk simulations can easily be modified to be run in 3D, the agreement in fractal dimension with the 2D imaging suggests that a 2D model is sufficient. Similar to how the fractal dimension of the fingering pattern is correlated with the capillary number, we have determined that the fractality of the fingering-like patterns visible in the cell migration patterns also follow the similar relationship between fractality and parameters analogous to capillary number [36]. Therefore, we estimate that the differential affinity, which is roughly analogous to the interfacial tension in a fluid–fluid boundary, is inversely correlated with the fractal dimension of the cell–cell boundary layer.

Our findings suggest that the differential affinity between cells of different origins play a crucial role in cell organization and boundary formation, which seems to suggest differential adhesion hypothesis (DAH) first introduced by Twomes and Holtfreter in their landmark 1955 study [49]. Since then, numerous studies have reported on the effects of differential adhesion on the formation of cell aggregate boundaries, which can be modeled to be liquid-like. Varying the cadherin levels in L cell aggregates have affected the segregation and sorting of cells guided by free energy of cell–cell binding [9]. In another study, Toll1, a transmembrane protein that plays a role in intercellular adhesion, has been shown to correct distortions in *Drosophila* pupa epidermal epithelium, further supporting the DAH [50]. However, DAH has been a controversial subject in the field of tissue engineering and developmental biology, with some studies disputing the validity of modeling cell aggregates as immiscible fluids and suggesting dynamic factors in addition to differential adhesion may play a significant role in cell organization [51, 52]. Our findings endorses the validity of DAH in the self-organizing behavior of BECs and LECs as well as

put forth a new mathematical approach to model the cell–cell boundary behavior. Future studies should explore the use of various grid coarseness in our random walk simulations to fully confirm that the cell–cell boundary can be modeled accurately as a continuum similarly to partially miscible fluids despite the significantly larger size of each ‘particle’.

Overall, our findings indicate that the fractality measurement can be a simple tool to estimate the differential affinity in two groups of cells, which is useful in co-cultured tissue engineering where two or more types of cells must self-organize to form structures [2, 22]. Future studies could explore the use of this tool in various types of cells that may exhibit differential affinity, for example in tumor cells that attract endothelial cells for vessel formation [53, 54]. Our random walk simulation model could also be applied to predict the formation of blood vessels in vascularized organoids, where mobile endothelial cells invade a less mobile group of cells to form perfusing vessels [55, 56]. Taken together, our fractality tool is a novel approach to measure the differential affinity between cells that does not require protein level analysis, which can have a broad application in cell development and tissue engineering.

Future studies should explore the limitations and potential sources of error in the methods used in this study. While box-counting method is a widely used method for estimating fractal dimensions, it suffers from quantization error, which stems from variabilities in grid orientation and placement as well as scaling range [57]. In order to reduce the effect of the errors in box-counting method, we determined the linear region over various box scaling ranges, but improvements on the box counting method such as pattern search which have higher computational cost could be applied in future studies [58]. Additionally, we included five variable parameters in the random walk simulations in order to potentially model the variabilities in cell motility characteristics, but for the simplicity of our mathematical derivations we only tested the effect of varying a_d which subsequently varies our simulated interfacial tension. Future studies using our random walk simulation could explore the effects of varying migration potential and the a_l parameters to fully capture the dynamics between various cell lines.

Data availability statement

The data that support the findings of this study are openly available at the following URL/DOI: <https://github.com/donghyunjeong21/FractalityOfCellBoundary>.

Acknowledgments

We acknowledge support from the University of Notre Dame through ‘Advancing Our Vision’

Initiative in Stem Cell Research, Harper Cancer Research Institute—American Cancer Society Institutional Research Grant (IRG-17-182-04), American Heart Association through Career Development Award (19-CDA-34630012 to D H-P), National Institutes of Health (1R35-GM-143055-01 to D H-P), National Science Foundation (NSF GRFP to D P J and 2225601 to D H-P and H-C C), and Center for Bioanalytic and Metrology NSF/Industry grant to H-C C and D H-P.

Conflict of interest

The authors have declared that no conflict of interest exists.

Author contributions

D P J, D M P, H-C C and D H-P conceived the ideas, designed the experiments, interpreted the data, and wrote the manuscript. D P J wrote the code and performed the computational modeling. H-C C and D H-P supervised the study. All authors have approved the manuscript.

ORCID iDs

Donghyun Paul Jeong  <https://orcid.org/0000-0002-5502-1752>

Hsueh-Chia Chang  <https://orcid.org/0000-0003-2147-9260>

Donny Hanjaya-Putra  <https://orcid.org/0000-0002-5403-544X>

References

- [1] Oliver G 2004 Lymphatic vasculature development *Nat. Rev. Immunol.* **4** 35
- [2] Smith Q, Rochman N, Carmo A M, Vig D, Chan X Y, Sun S and Gerecht S 2018 Cytoskeletal tension regulates mesodermal spatial organization and subsequent vascular fate *Proc. Natl Acad. Sci.* **115** 8167–72
- [3] Kazenwadel J and Harvey N L 2016 Morphogenesis of the lymphatic vasculature: a focus on new progenitors and cellular mechanisms important for constructing lymphatic vessels *Dev. Dyn.* **245** 209–19
- [4] González-Ramírez M C, Guzmán-Palma P and Oliva C 2021 Cell segregation and boundary formation during nervous system development *Int. J. Dev. Biol.* **65** 251–61
- [5] Ingber D E 2002 Mechanical signaling and the cellular response to extracellular matrix in angiogenesis and cardiovascular physiology *Circ. Res.* **91** 877–87
- [6] Nelson C M, VanDuijn M M, Inman J L, Fletcher D A and Bissell M J 2006 Tissue geometry determines sites of mammary branching morphogenesis in organotypic cultures *Science* **314** 298
- [7] Larue L, Ohsugi M, Hirchenhain J and Kemler R 1994 E-cadherin null mutant embryos fail to form a trophoblast epithelium *Proc. Natl Acad. Sci. USA* **91** 8263–7
- [8] Betterman K L *et al* 2020 Atypical cadherin FAT4 orchestrates lymphatic endothelial cell polarity in response to flow *J. Clin. Invest.* **130** 3315–28
- [9] Foty R A and Steinberg M S 2005 The differential adhesion hypothesis: a direct evaluation *Dev. Biol.* **278** 255–63

- [10] Amack J D and Manning M L 2012 Knowing the boundaries: extending the differential adhesion hypothesis in embryonic cell sorting *Science* **338** 212–5
- [11] Stoykova A, Gotz M, Gruss P and Price J 1997 Pax6-dependent regulation of adhesive patterning, R-cadherin expression and boundary formation in developing forebrain *Development* **124** 3765–77
- [12] Inoue T, Tanaka T, Takeichi M, Chisaka O, Nakamura S and Osumi N 2001 Role of cadherins in maintaining the compartment boundary between the cortex and striatum during development *Development* **128** 561–9
- [13] McMillen P, Chatti V, Jülich D and Holley S A 2016 A sawtooth pattern of cadherin 2 stability mechanically regulates somite morphogenesis *Curr. Biol.* **26** 542–9
- [14] Cayuso J, Xu Q and Wilkinson D G 2015 Mechanisms of boundary formation by Eph receptor and ephrin signaling *Dev. Biol.* **401** 122–31
- [15] Taylor H B, Khuong A, Wu Z, Xu Q, Morley R, Gregory L, Poliakov A, Taylor W R and Wilkinson D G 2017 Cell segregation and border sharpening by Eph receptor–ephrin-mediated heterotypic repulsion *J. R. Soc. Interface* **14** 20170338
- [16] Landsberg K P, Farhadifar R, Ranft J, Umetsu D, Widmann T J, Bittig T, Said A, Jülicher F and Dahmann C 2009 Increased cell bond tension governs cell sorting at the drosophila anteroposterior compartment boundary *Curr. Biol.* **19** 1950–5
- [17] McClatchey A I 2021 EPHecting cell contact by increasing cortical tension *J. Cell Biol.* **220** e202105015
- [18] Battle E and Wilkinson D G 2012 Molecular mechanisms of cell segregation and boundary formation in development and tumorigenesis *Cold Spring Harb. Perspect. Biol.* **4** a008227–a008227
- [19] Burroughs N J and Wülfing C 2002 Differential segregation in a cell–cell contact interface: the dynamics of the immunological synapse *Biophys. J.* **83** 1784–96
- [20] Sinnecker D, Laugwitz K-L and Moretti A 2014 Induced pluripotent stem cell-derived cardiomyocytes for drug development and toxicity testing *Pharmacol. Ther.* **143** 246–52
- [21] Hanjaya-Putra D, Bose V, Shen Y-I, Yee J, Khetan S, Fox-Talbot K, Steenbergen C, Burdick J A and Gerecht S 2011 Controlled activation of morphogenesis to generate a functional human microvasculature in a synthetic matrix *Blood* **118** 804–15
- [22] Kusuma S, Shen Y-I, Hanjaya-Putra D, Mali P, Cheng L and Gerecht S 2013 Self-organized vascular networks from human pluripotent stem cells in a synthetic matrix *Proc. Natl Acad. Sci.* **110** 12601–6
- [23] Alderfer L, Russo E, Archilla A, Coe B and Hanjaya-Putra D 2021 Matrix stiffness primes lymphatic tube formation directed by vascular endothelial growth factor-C *FASEB J.* **35** e21498
- [24] Hooks J S T, Bernard F C, Cruz-Acuña R, Nepiyushchikh Z, Gonzalez-Vargas Y, García A J and Dixon J B 2022 Synthetic hydrogels engineered to promote collecting lymphatic vessel sprouting *Biomaterials* **284** 121483
- [25] Abaci H E, Coffman A, Doucet Y, Chen J, Jacków J, Wang E, Guo Z, Shin J U, Jahoda C A and Christiano A M 2018 Tissue engineering of human hair follicles using a biomimetic developmental approach *Nat. Commun.* **9** 5301
- [26] Song W et al 2019 Engineering transferrable microvascular meshes for subcutaneous islet transplantation *Nat. Commun.* **10** 4602
- [27] Mukhtar N, Cytrynbaum E N and Edelstein-Keshet L 2022 A multiscale computational model of YAP signaling in epithelial fingering behavior *Biophys. J.* **121** 1940–8
- [28] Mark S, Shlomovitz R, Gov N S, Poujade M, Grasland-Mongrain E and Silberzan P 2010 Physical model of the dynamic instability in an expanding cell culture *Biophys. J.* **98** 361–70
- [29] Köpf M H and Pismen L M 2013 A continuum model of epithelial spreading *Soft Matter* **9** 3727
- [30] Ercolini E, Valle F, Adamcik J, Witz G, Metzler R, De Los Rios P, Roca J and Diéler G 2007 Fractal dimension and localization of DNA knots *Phys. Rev. Lett.* **98** 058102
- [31] Yang L, Zhang D, Zhang X and Tian A 2021 Surface profile topography of ionic polymer metal composite based on fractal theory *Surf. Interfaces* **22** 100834
- [32] Leggett S E, Neronha Z J, Bhaskar D, Sim J Y, Perdikari T M and Wong I Y 2019 Motility-limited aggregation of mammary epithelial cells into fractal-like clusters *Proc. Natl Acad. Sci. USA* **116** 17298–306
- [33] Jelinek H F and Fernandez E 1998 Neurons and fractals: how reliable and useful are calculations of fractal dimensions? *J. Neurosci. Methods* **81** 9–18
- [34] Cannon J W and Mandelbrot B B 1984 The fractal geometry of nature *Am. Math. Mon.* **91** 594
- [35] Zamir M 1999 On fractal properties of arterial trees *J. Theor. Biol.* **197** 517–26
- [36] Thamida S K, Takhistov P V and Chang H-C 2001 Fractal dewetting of a viscous adhesive film between separating parallel plates *Phys. Fluids* **13** 2190–200
- [37] Céspedes S, Molina A, Lerner B, Pérez M S, Franco C A and Cortés F B 2021 A selection flowchart for micromodel experiments based on computational fluid dynamic simulations of surfactant flooding in enhanced oil recovery *Processes* **9** 1887
- [38] Lee J, Huang J and Babadagli T 2022 Viscous fingering during heavy-oil displacement by chemical solutions: emulsion instability and partial-miscibility *J. Pet. Sci. Eng.* **209** 109954
- [39] Guo H, Dou M, Hanqing W, Wang F, Yuanyuan G, Yu Z, Yansheng W and Li Y 2017 Proper use of capillary number in chemical flooding *J. Chem.* **2017** 1–11
- [40] Nittmann J, Daccord G and Stanley H E 1985 Fractal growth viscous fingers: quantitative characterization of a fluid instability phenomenon *Nature* **314** 141–4
- [41] Jeong D P, Hall E, Neu E and Hanjaya-Putra D 2022 Podoplanin is responsible for the distinct blood and lymphatic capillaries *Cell Mol. Bioeng.* **15** 467–78
- [42] Hanjaya-Putra D, Yee J, Ceci D, Truitt R, Yee D and Gerecht S 2010 Vascular endothelial growth factor and substrate mechanics regulate *in vitro* tubulogenesis of endothelial progenitor cells *J. Cell. Mol. Med.* **14** 2436–47
- [43] Stringer C, Wang T, Michaelos M and Pachitariu M 2021 Cellpose: a generalist algorithm for cellular segmentation *Nat. Methods* **18** 100–6
- [44] Schacht V et al 2003 T1 α /podoplanin deficiency disrupts normal lymphatic vasculature formation and causes lymphedema *EMBO J.* **22** 3546–56
- [45] Bertozzi C C et al 2010 Platelets regulate lymphatic vascular development through CLEC-2–SLP-76 signaling *Blood* **116** 661–70
- [46] Osada M et al 2012 Platelet activation receptor CLEC-2 regulates blood/lymphatic vessel separation by inhibiting proliferation, migration, and tube formation of lymphatic endothelial cells *J. Biol. Chem.* **287** 22241–52
- [47] Bui L et al 2022 Engineering bioactive nanoparticles to rejuvenate vascular progenitor cells *Commun. Biol.* **5** 635
- [48] Patmonoaji A, Muharrik M, Hu Y, Zhang C and Suekane T 2020 Three-dimensional fingering structures in immiscible flow at the crossover from viscous to capillary fingering *Int. J. Multiph. Flow* **122** 103147
- [49] Townes P L and Holtfreter J 1955 Directed movements and selective adhesion of embryonic amphibian cells *J. Exp. Zool.* **128** 53–120
- [50] Iijima N, Sato K, Kuranaga E and Umetsu D 2020 Differential cell adhesion implemented by *Drosophila* Toll corrects local distortions of the anterior-posterior compartment boundary *Nat. Commun.* **11** 6320
- [51] Pawlizak S et al 2015 Testing the differential adhesion hypothesis across the epithelial–mesenchymal transition *New J. Phys.* **17** 083049

- [52] Tambe D T and Fredberg J J 2015 And I hope you like jamming too *New J. Phys.* **17** 091001
- [53] Ngo M T and Harley B A 2017 The influence of hyaluronic acid and glioblastoma cell coculture on the formation of endothelial cell networks in gelatin hydrogels *Adv. Healthcare Mater.* **6** 1700687
- [54] Ozturk M S, Lee V K, Zou H, Friedel R H, Intes X and Dai G 2020 High-resolution tomographic analysis of *in vitro* 3D glioblastoma tumor model under long-term drug treatment *Sci. Adv.* **6** eaay7513
- [55] Wimmer R A *et al* 2019 Human blood vessel organoids as a model of diabetic vasculopathy *Nature* **565** 505–10
- [56] Hanjaya-Putra D, Wong K T, Hirotsu K, Khetan S, Burdick J A and Gerecht S 2012 Spatial control of cell-mediated degradation to regulate vasculogenesis and angiogenesis in hyaluronan hydrogels *Biomaterials* **33** 6123–31
- [57] Jiang S and Liu D 2012 Box-counting dimension of fractal urban form: stability issues and measurement design *Int. J. Artif. Life Res.* **3** 41–63
- [58] Bouda M, Caplan J S and Saiers J E 2016 Box-counting dimension revisited: presenting an efficient method of minimizing quantization error and an assessment of the self-similarity of structural root systems *Front. Plant Sci.* **7** 149